

Ultrafast Bubble Bursting by Superamphiphobic Coatings

Katharina I. Hegner, William S. Y. Wong,* and Doris Vollmer*

Controlling bubble motion or passively bursting bubbles using solid interfaces is advantageous in numerous industrial applications including flotation, catalysis, electrochemical processes, and microfluidics. Current research has explored the formation, dissolution, pinning, and rupturing of bubbles on different surfaces. However, the ability to tune and control the rate of bubble bursting is not yet achieved. Scaling down surface-induced bubble bursting to just a few milliseconds is important for any application. In this work, the hierarchical structure of superamphiphobic surfaces is tuned in order to rapidly rupture contacting bubbles. Surfaces prepared using liquid flame spray show ultrafast bubble bursting (down to 2 ms) and superior durability. The coatings demonstrate excellent mechanical and chemical stability even in the presence of surface-active species. Air from the ruptured bubble is absorbed into the aerophilic Cassie-state. Long-term applicability is demonstrated by preventing the accumulation of air in the plastron via a connection of the plastron to the environment. The times recorded for bubble rupture and complete reorganization of air are reduced by approximately a factor of 3 compared to previously reported values. The concept is utilized to passively control surfactant-rich foam in froth flotation. Material collection efficiency increased by more than 60 times compared to controls.

1. Introduction

Bubble attachment and accumulation challenge a wide variety of industrial applications. For instance, in the fast-growing field of electrocatalysis for clean energy production, gas bubbles evolving on the electrodes block the effective catalytic sites.^[1–4] At a larger scale, the chemical, water, and food processing industry often face the challenge of foam accumulation, which can lead to processing problems and reduced product yields.^[5–7] In froth flotation, used in wastewater treatment^[8,9] and mineral-mining industries,^[10,11] control of air bubbles and froth carrying hydrophobic particles from a slurry is essential for facilitating a cost-effective separation process.^[7] Therefore, methods to improve control of rapid bubble bursting or froth are highly desirable.

K. I. Hegner, Dr. W. S. Y. Wong, Prof. D. Vollmer
Physics at Interfaces
Max Planck Institute for Polymer Research
Ackermannweg 10, 55128 Mainz, Germany
E-mail: wong@mpip-mainz.mpg.de; vollmerd@mpip-mainz.mpg.de

 The ORCID identification number(s) for the author(s) of this article can be found under <https://doi.org/10.1002/adma.202101855>.

© 2021 The Authors. Advanced Materials published by Wiley-VCH GmbH. This is an open access article under the terms of the Creative Commons Attribution-NonCommercial-NoDerivs License, which permits use and distribution in any medium, provided the original work is properly cited, the use is non-commercial and no modifications or adaptations are made.

DOI: 10.1002/adma.202101855

Current research has focused mainly on understanding bouncing,^[12] pinning,^[13,14] spreading,^[15,16] and the transport^[3,17] of bubbles. Wang et al. demonstrated bubble bursting and absorption on artificial hierarchical lotus leaves within tens of milliseconds.^[18] On the contrary, on dense superhydrophobic nanowires, the bubble remained pinned. Rapoport et al. showed that localized microscale protrusions allow faster drainage of the liquid film separating the bubble and the protrusion.^[12] When combined, these studies suggest that a hierarchical and microscopically rough texture is vital towards achieving ultrafast bubble capture.^[12,18] Current state-of-the-art surfaces remain comparatively slow in bubble capture (approximately 13 ms)^[12,18] and are seemingly at their performance limit. Scalable coating methods with long-term performance are required for industrial applications. Furthermore, the mechanism for passively inducing ultrafast bubble bursting and air absorption is still unclear.

Film thinning models suggest that features should be as small as possible to enhance bubble bursting.^[19] The required tunable nanoscale architectures were not easily attained, until the recent advent of liquid flame spray (LFS)-based superhydrophobic /superamphiphobic surfaces.^[20,21] LFS is an extremely fast and versatile coating technique that allows for tuning of surface structures and contacting protrusions at the micro- and nano-scale.^[20–24] Therefore, it enables a deeper investigation into the surface morphology required for ultrafast bubble bursting.

Here, we present the design principles of surface-immobilized aerophilic superamphiphobic coatings capable of ultrafast passive bubble bursting. Superamphiphobic coatings produced via LFS are benchmarked against surfaces developed by wet-spray coating and superhydrophobic silicone nanofilaments (SNF). On optimized LFS coatings, bubbles were fully absorbed and reorganized by the aerophilic structures in less than 4 ms after contact in water. Compared to previously reported results, we were able to reduce the time required for bubble rupture and air absorption by approximately a factor of 3.^[12,18] In C12E5 soap solution, bubble rupturing required a maximum of 75 ms. Long-term performance was demonstrated by providing a continuous pathway for excess air to escape into the environment.

Rough porous microstructures coupled to the smallest possible particulate nanostructures with diameters below 100 nm appear to provide the optimal surface properties for ultrafast bubble rupture. We applied these findings to passively control froth flotation and increased the material collection efficiency by more than 60 times.

2. Results and Discussion

To understand the influence of surface morphology and topography on bubble bursting, we fabricated superamphiphobic and superhydrophobic model surfaces based on particulate or fibrous structures (Figure S1, Supporting Information).

On a superhydrophobic surface, only the very tips of the surface structures (i.e., protrusions) are in contact with water. Superhydrophobicity is achieved by a combination of surface roughness and low surface energy.^[25,26] By introducing overhanging, so-called re-entrant geometries, superamphiphobic surfaces are able to repel even low-surface-tension liquids.^[27,28] When immersed in a liquid, the plastron (air layer) renders the surface aerophilic.^[16]

Particle coatings were produced either via LFS or by wet-spray coating, hereafter called LFS (Figure 1a–d) and dense nanoparticle (DNP) coating^[29] (Figure 1e), respectively. For comparison, fibrous SNF^[30,31] were investigated (Figure 1f).

Unlike many other coating techniques, LFS allows for the precise control of particle size and coating morphology by tuning the process parameters.^[20,22–24] A liquid feedstock containing the precursor, here tetraethoxysilane (TEOS) in isopropanol, is injected into a process gas flame (Figure 1g, Experimental Section for details). After evaporation of the liquid phase, the precursor reacts and nucleates in the flame. Depending on the residence time of the particles in the flame, they grow, agglomerate, and sinter until they arrive at the substrate.^[32,33] The deposition mechanism of the nanoparticles into porous, 3D microstructures is controlled by the Peclet number, that is, the scaled ratio between the orthogonal/advective velocity and the stochastically distributed diffusive velocity caused by Brownian motion.^[34,35] Independent of the deposition regime, the primary particle size and degree of particle aggregation influence the mobility of particles/particle aggregates and therefore, the morphology of the resulting film.^[36] For more information on particle formation and assembly in LFS, see Supporting Information.

Here, the morphology of resulting silicone dioxide coatings is tuned by varying the position of the substrate with respect to the burner (d_{burner}) and the coating time. Decreasing the coating distance from 52 to 22 cm at a constant coating time of 10 min led to an increase in film thickness from approximately 20 to 75 μm (Figure 1a–d). After 10 min, the one-step coating process started to show a two-tier structure: the bottom layer remains porous but macroscopically flat while the top layer constitutes of cone-shaped structures (Figure 1a–d). With decreasing coating distance, the structures become more pronounced. This effect is observed for coating distances as low as 12 cm (Figure S2, Supporting Information). The variation of other process parameters such as increasing the precursor feed rate or reducing the precursor concentration does not lead to the formation of the characteristic two-tier structures. Instead, macroscopically flat films are formed (Figure S3, Supporting Information).

To stabilize the porous structures and to improve adhesion with the substrate, a silica shell was deposited by chemical vapor deposition (CVD) of TEOS.^[37] The surface energy was lowered by fluoro-functionalization via CVD. Independent of the LFS process parameters, all surfaces show exceptional wetting

properties with roll-off angles for low-surface-tension *n*-hexadecane (275 mN m^{-1} , 6 μL) of $< 2^\circ$ (Figure 1h). Figure 1e shows a surface prepared by wet-spray coating of fluoro-functionalized silicone dioxide nanoparticles.^[29] During wet-spray coating, the functionalized particles formed aggregates with a diameter of 62 ± 13 nm. Compared to LFS coatings, much denser geometries can be discerned, hence the term DNP coating. The wetting properties of the DNP surface are comparable to the porous LFS nanoparticle coatings, that is, *n*-hexadecane drops roll off when tilting the surface by approximately 3° . To produce superhydrophobic SNF, a glass slide was immersed in a solution containing trichloromethylsilane (TCMS) and toluene with trace amounts of water.^[30] The resulting fibers have a diameter of 33 ± 13 nm (Figure 1f). Upon fluoro-functionalization, the roll-off angle for *n*-hexadecane is $24^\circ \pm 3^\circ$.

We immersed the surfaces into environmentally-equilibrated milli-Q water or C12E5 surfactant solution. The distance between the needle and the surface was fixed at 2.5 mm. A bubble with a radius of 0.9 mm was produced using a syringe pump. We recorded bubble impact using a high-speed camera (Figure 1i). The bubble was then tracked using custom image-processing algorithms (edge detection) in MATLAB, where the velocity of the 2D center-of-mass was computed. The bubble approached the surface with a velocity of up to 0.14 m s^{-1} . From the bubble velocity, we reconstructed the moment of the first contact between the bubble and the surface, corresponding to the minimum decelerated velocity (Figure 1j). We define this time as t_0 . The sharp increase in velocity detected when the bubble is ruptured by the surface, followed by rapid absorption of air by the coating, is defined as t_1 . At t_1 , air from the ruptured bubble is absorbed by the surface but not yet fully reorganized (see second to last optical image in Figure 1i). The rupturing time t_r is the difference between t_1 and t_0 and is used as a quantitative measure of the bubble bursting property of a surface.

In Figure 1j, two possible scenarios are depicted (Videos M1 and M2, Supporting Information). The red dataset depicts the velocity of a bubble that bounces off a surface multiple times. Bubble rebound corresponds to negative velocities. Finally, the bubble slows down and eventually comes to rest. After 175 ms, the bubble ruptures spontaneously. The air is rapidly absorbed into the air layer within the surface structures, resulting in a sharp increase in velocity. The blue dataset shows the case of a surface inducing bubble bursting immediately upon contact, so-called ultrafast bubble bursting. The bubble does not even slow down to zero velocity before rupture (see inset). Bubble rupturing requires less than 2 ms. Only 4 ms after the first bubble-to-surface contact, the air is fully absorbed and reorganized by the structure (see last optical image in Figure 1i). For standard bubbles with a radius of 0.9 mm and optimized surfaces, ultrafast bubble bursting ($t_r < 2$ ms) is observed in more than 90 % of the experiments.

The rate at which air is absorbed into the structures is independent of the rupturing time and the type of surface used (see Figure S4, Supporting Information, for velocity graphs). For bubbles with a radius of 0.2 mm, even faster bubble bursting is observed. The rupturing time varies between 0.5 and 1.0 ms. Here, the maximum velocity of air absorption (center of mass velocity) is lower. This can be attributed to the comparatively low volume of air to be absorbed (Figure S5 and Video M3, Supporting Information).

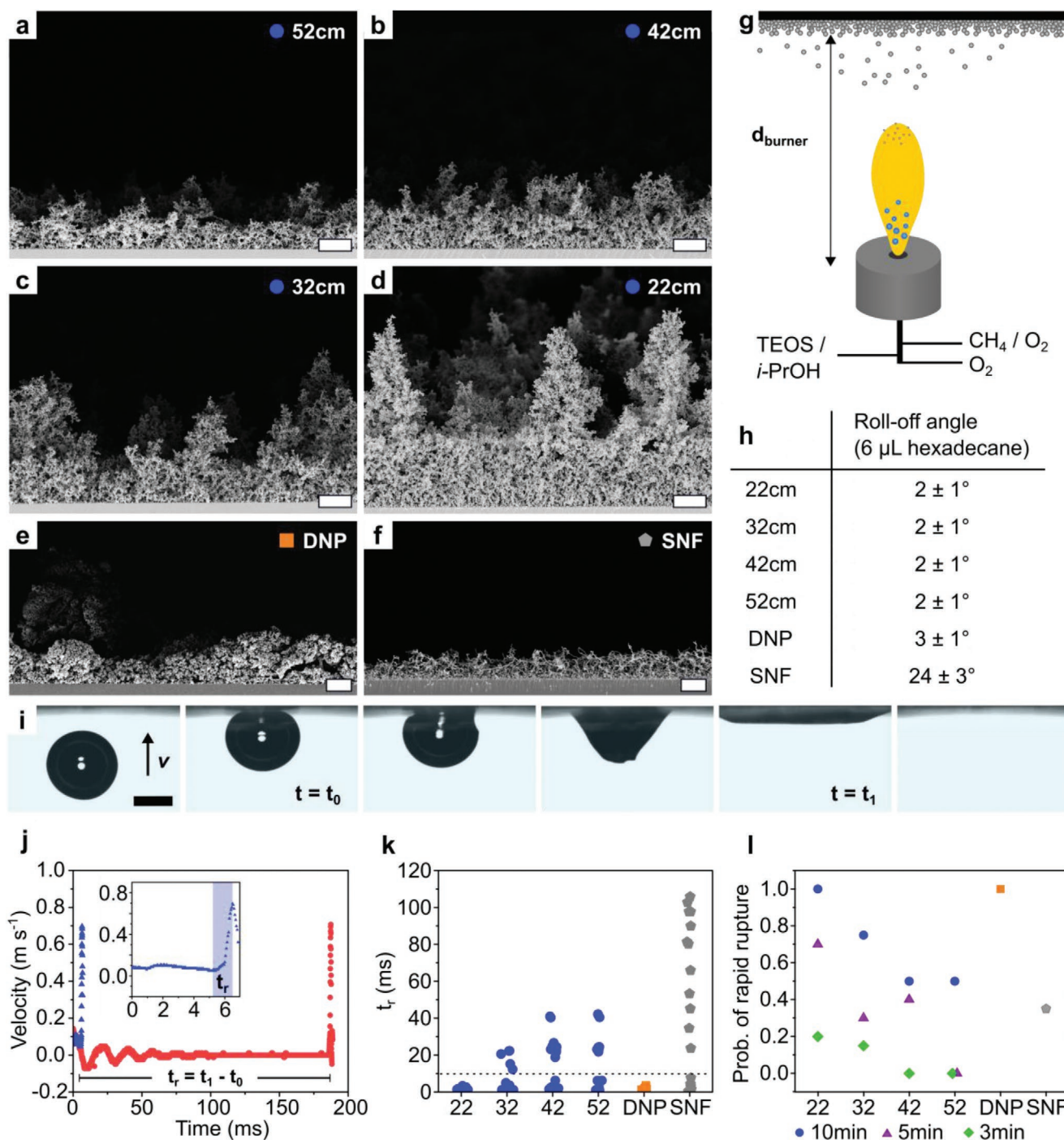


Figure 1. Side-view SEM images of a–d) LFS surfaces coated at different distances to the burner for 10 min (scale bars are 10 μm), e) a dense nanoparticle coating, DNP (scale bar is 2 μm), and f) silicone nanofilaments, SNF (scale bar is 2 μm). g) Schematic illustration of the LFS setup (not to scale). h) Roll-off angles using 6 μL droplets of *n*-hexadecane as a probe liquid. i) Images acquired by a high-speed camera (scale bar is 1 mm) showing an air bubble rupturing immediately upon contacting the surface. j) Bubble velocity as a function of time, depicting two different scenarios of how 1) a bubble ruptures immediately upon impact (blue dataset, inset) and 2) a bubble may also bounce off a surface multiple times before coming to rest and finally rupturing spontaneously (red dataset). k) Rupturing times of bubbles rising in water against 20 different spots on pristine surfaces. l) Probability of rapid rupture (<10 ms) upon the first contact.

Figure 1k depicts the time required for bubbles to rupture upon contacting LFS surfaces (blue circles) produced at different coating distances (d_{burner}), as well as the single-configuration DNP (orange square) and SNF surfaces (grey

pentagons). A minimum of 20 experiments (i.e., 20 different spots) was conducted per surface. After each bubble, the surface was removed from the liquid, allowing dissipation of absorbed air.

We observe an influence of LFS process parameters on the bubble rupturing time, t_r . Bubbles with varying diameters contacting a surface coated for 10 min at 22 cm distance to the burner always rupture immediately upon first contact with rupturing times well below 10 ms (see dotted line in Figure 1k and Figure S5, Supporting Information). For coating distances exceeding 22 cm, bubbles can rebound and oscillate, as reflected by the time intervals between data clusters. Surfaces coated at 52 cm distance induce rupturing upon first contact in only 50 % of all experiments.

To provide additional insight on the effect of coating thickness and morphology, we decreased LFS coating times from 10, to 5, and 3 min and the coating distance from 52 to 22 cm (see Figures S6 and S7, Supporting Information, for surface morphology and Figure S8, Supporting Information, for t_r at different coating times). Unlike LFS coatings, DNP and SNF surfaces are not tunable.

To facilitate a concise comparison between all surfaces, we calculated the probability of rapid rupture (Figure 1l). We define rapid rupture as a t_r of less than 10 ms upon first contact between the bubble and the surface (see dotted line in Figure 1k). For LFS coatings, the probability of rapid rupture increases with increasing coating time and decreasing coating distance (Figure 1l). Per Figure 1k,l, the DNP coating (orange squares)

also shows bubble rupturing well below 10 ms. Compared to nanoparticles, the smoother nanofilaments (grey pentagons) are less suitable for consistently reliable rapid bubble rupturing. A larger bubble-to-surface contact area and higher flexibility of the nanofilaments might have caused rupturing times ranging from 2 to 110 ms. This hints that sharp particulate structures are favorable. Based on these results, it appears that the macroscopic morphology of the coating and the size of individual particles both play crucial roles in inducing bubble rupturing.

To understand the relation between the hierarchical structures and bubble rupturing, we investigated the influence of process conditions on LFS coatings. The size of individual nanoparticles is expected to increase with increasing coating distance due to a longer residence time of particles in the hot zone. This allows particles to further grow and sinter.^[22,24] Indeed, we observe a trend in particle diameter with the coating distance (Figure 2a,b). The particle diameter decreased from 126 ± 18 to 79 ± 14 nm when the coating distance was reduced from 52 to 22 cm (after addition of a silica shell via CVD). The DNP coating is composed of nanoparticle aggregates with a diameter of 62 ± 13 nm (Figure 2c). This hints that the effective bubble rupturing capabilities of LFS (22 cm) and DNP surfaces are caused by the ultrafine nanoparticle and nanoparticle aggregate diameter, respectively.

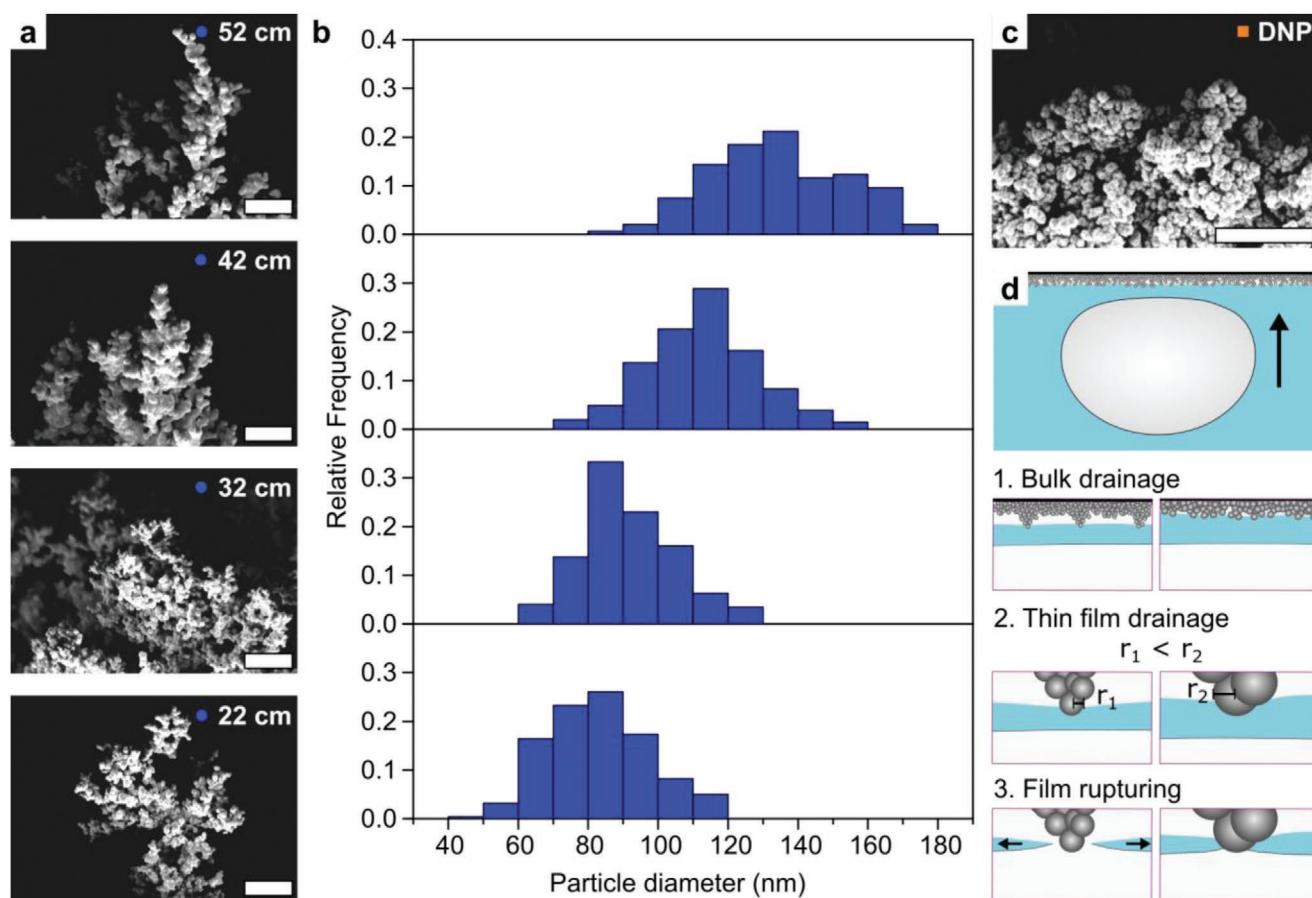


Figure 2. Effect of surface morphology on bubble rupturing. a) Side-view SEM images of LFS surfaces coated at decreasing distances to the burner (scale bars are 1 μm) and b) corresponding particle size distributions. c) Side-view SEM image of a DNP surface (scale bar is 1 μm). d) Schematic illustration of the bubble rupturing mechanism on nanoparticles with $r_1 < r_2$ (not to scale).

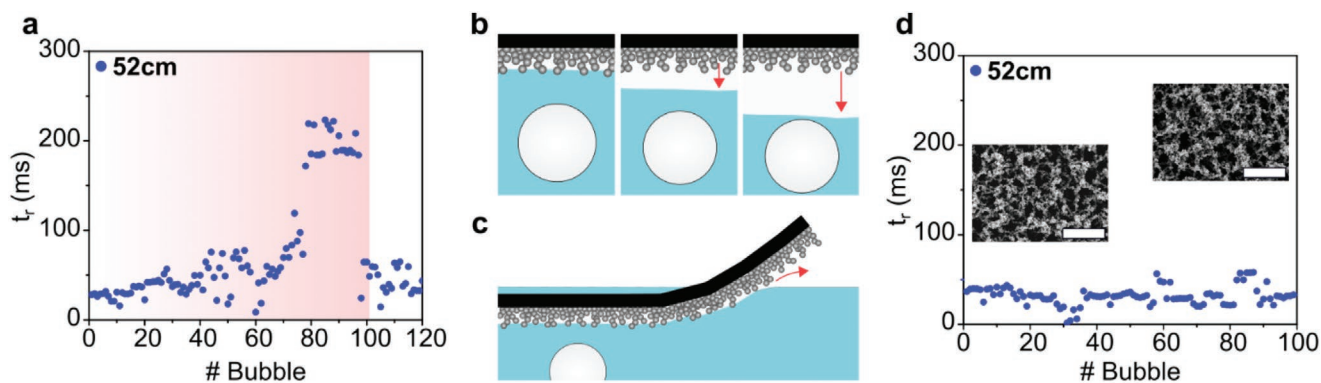


Figure 3. Long-term stability. a) Rupturing times of 120 consecutive bubbles on an LFS coating. To highlight the effect of air layer build-up, a surface coated for 10 min at a distance of 52 cm was used for exemplification. After 100 bubbles, the captured air was allowed to escape. b) Schematic illustration of a superamphiphobic particle surface fully submerged in a liquid. The air layer gradually builds up in thickness with the addition of air from each consecutive bubble (not to scale). c) Schematic illustration of a bent surface where the air layer within the coating is connected to the environment. The air from captured bubbles is continuously released into the environment, thus preserving surface performance. d) Rupturing times of 100 consecutive bubbles on a bent LFS coating (52 cm, 10 min) connected to the ambient gaseous environment. SEM images before and after the experiment show no mechanical degradation (scale bars are 10 μm).

These observations raise the question, how the tunable nanoscale configuration influences the time required for bubble rupturing. In the left panels in Figure 2d, the bubble approaches a coating with prominent surface protrusions made up of particles with radii r_1 . In contrast, the right panels illustrate larger nanoparticles with radii r_2 , where $r_2 > r_1$.

Upon bulk drainage, film thinning between the flattened bubble and the surface continues. The deformation of the bubble due to the proximity of the surface protrusions can be described by an augmented Young–Laplace equation (see Supporting Information).^[19] The liquid film is confined between air from the bubble and protrusions constituting the aerophilic surface. The smaller the protrusions, the higher the imposed pressure gradient which increases the force pushing liquid out of the thin film. Additionally, less liquid needs to be moved from in-between the bubble and individual protrusions.^[38] The hydrodynamic drainage of the thin film can be described by the Stokes–Reynolds equation.^[19,39] Eventually, one or multiple particle protrusions pierce the film and establish a three-phase contact line with the bubble. As soon as a particle pierced the film, a pressure gradient in the film within close proximity of the particle pushes the liquid away. The three-phase contact line of the bubble’s air-liquid-solid interface migrates along the particle surface, maintaining its receding contact angle. Eventually, the film has thinned sufficiently that the two contact lines meet and merge (see last panels in Figure 2d). In this secondary process of contact line motion, the individual particle size also influences the rupturing time: a smaller particle circumference leads to a reduced length of the migrating contact line and hence, reduces possible pinning events. Our experimental findings concur with these coupled mechanisms, where bubble rupturing occurs faster on coatings having a distribution of smaller particles.^[38,40]

Apart from particle size, particle aggregation and hierarchy appear to influence bubble rupture. We tuned surface hierarchy by varying the coating times at constant coating distances, thus maintaining constant particle diameters. With shorter coating times, more uniform particle networks are observed

(Figures S6 and S7, Supporting Information). In contrast, highly porous protrusions become more pronounced with increasing coating times. The rougher, more widely dispersed hierarchical structures greatly reduce the solid-liquid contact area which increases the slip length and reduces the friction the liquid film experiences.^[25,41] This enhances the film thinning velocity and accordingly the rate at which contact lines of neighboring protrusion can meet and merge in case of multiple points of bubble rupture. In line with reduced rupture times, rough and widely dispersed protrusions increase the probability of a bubble contacting individual particles or smaller particle aggregates, facilitating to pierce the liquid film. Collectively, these parameters reduce the bubble bursting time and allow faster absorption of the bubble into the surface structures.

Although these results are highly promising, one might speculate about the long-term performance of such coatings because of the gradual accumulation of air from ruptured bubbles. To understand the consequences of air accumulation within the coating (i.e., an increased thickness of the air plastron), bubbles were repeatedly ruptured in the same location. The captured air was not removed between tests. To visualize the effect, results for a sub-optimal LFS coating produced at a distance of 52 cm with a thickness of 20 μm are presented (Figure 3a). Conceptually, the same holds for the other investigated coating parameters and surface modifications (Figure S9, Supporting Information).

For the LFS coating presented here, the rupturing times increased with an increasing number of bubbles captured, from approximately 35 to 200 ms (Figure 3a and Figure S9, Supporting Information, for the performance of LFS coatings produced at different process conditions and single configuration DNP). With every rupturing event, air from the bubble is absorbed into the air layer of the superamphiphobic structure (Figure 3b). Each bubble adds an air volume of approximately 3 μL . The air layer gradually builds up in thickness, effectively preventing direct bubble-to-particle contact. Subsequent bubbles contacting this swollen air layer encounter a flexible interface that delays rupture, akin to bubble-to-bubble^[42] contact.

After absorbing 100 bubbles, the captured air was released into the environment. Thereafter, the surface recovered its rupturing time, demonstrating its functional durability (Figure 3a).

To resolve the influence of air layer build-up, a pathway for excess air to escape was introduced. We coated a glass slide with a 45° bend, as illustrated in Figure 3c. Figure 3d shows that t_r remained constant within experimental accuracy for all 100 captured bubbles (see Figure S10, Supporting Information, for the performance of an optimized LFS coating). We observe no mechanical degradation of the LFS coating after the impact and absorption of 100 consecutive bubbles (insets in Figure 3d). This highlights the durability and utility of such surfaces for long-term bubble capture.

In most real-world systems, surface-active species such as surfactants are present. Dissolved in an aqueous environment, they spontaneously adsorb at hydrophobic interfaces. To investigate the behavior of bubbles contacting an optimized LFS surface in the presence of a surface-active species, experiments were conducted using the nonionic surfactant pentaethylene glycol monododecyl ether (C12E5).^[43]

When immersed in water (purple), bubbles ruptured immediately upon contact with the LFS (Figure 4a) and DNP (Figure 4b) surfaces. Upon addition of C12E5 (red) at half the critical micelle concentration (0.03 mM, surface tension 30.7 mN m⁻¹),^[44] the time required for bubble rupturing on the LFS surface increased to 33 ± 21 ms. Bubbles did not bounce off the surface but rather rested on it until they spontaneously ruptured. Due to the presence of surfactant molecules at the liquid-gas and liquid-solid interfaces, the thin liquid film between the

two phases is temporarily stabilized. The molecules increase the elasticity of the thin film and reduce the Laplace pressure while increasing the pinning of the three-phase contact line, causing the overall increase in bubble rupturing times. SEM images before (Figure 4d) and after (Figure 4e) the experiment in soap solution show no mechanical degradation of the LFS coating. The LFS surface maintains its superamphiphobic wetting properties (Figure 4c). However, for the DNP surface, we observed delamination and partial imbibition of the coating starting with the impact of the first bubble and during the repeated release of captured air into the environment. While the DNP surface initially showed comparatively low rupturing times of 9 ± 8 ms, it eventually failed to induce bubble rupturing (Figure 4b, red area). After experiments in the C12E5 solution, only patchy particle aggregates remained on the substrate (Figure 4f,g). Interestingly, the damaged surface was able to retain superhydrophobic properties (Figure 4c). Drops of water and C12E5 solution rolled off when the surface was tilted by only a few degrees. The poorer durability of the DNP surface can be attributed to its lack of having a binder or adhesion promoter. A binder increases adhesion of the coating to the substrate, thus counteracting delamination.

The LFS surface is able to maintain its mechanical structure and superamphiphobic properties even after repeated bubble rupturing in the soap solution, demonstrating the superior performance of these surfaces.

The concept of passive surface-induced bubble bursting is not limited to single consecutive bubbles but can also be applied to bulk foams. The ability to rupture bubbles even in solutions

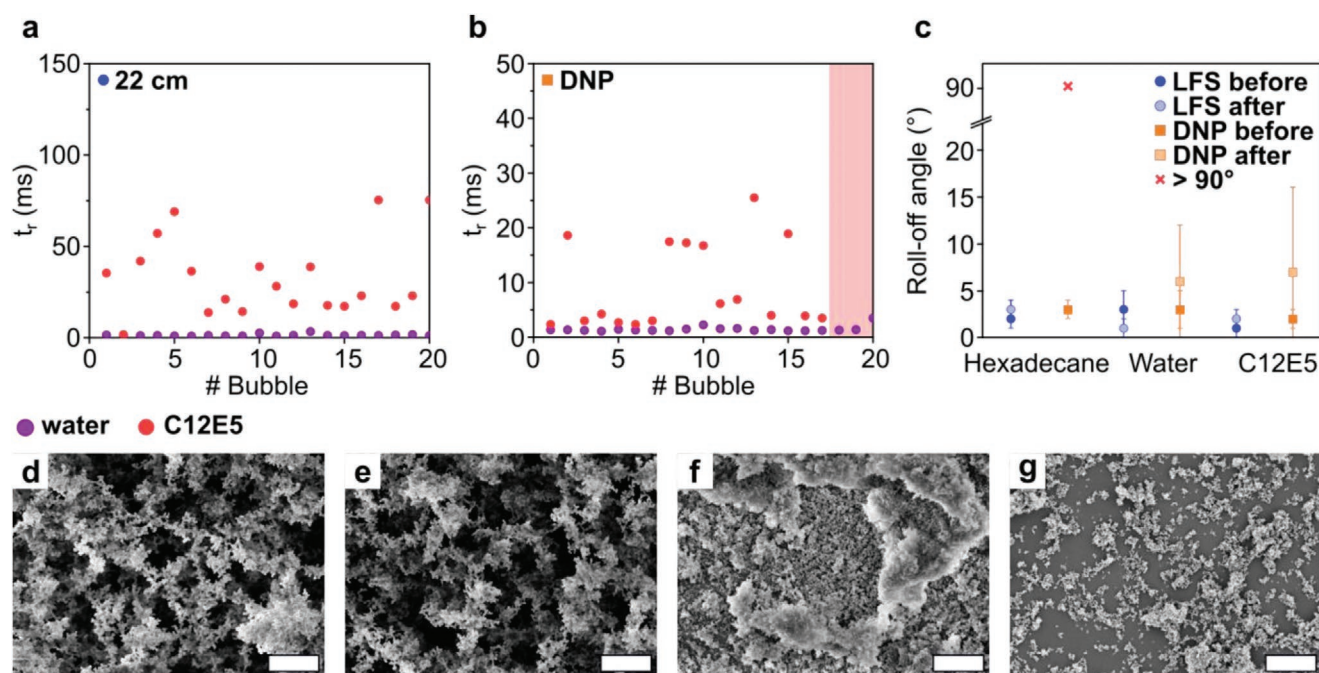


Figure 4. Surface-active species. Rupturing times of individual bubbles in 20 different spots on a) an LFS surface (22 cm, 10 min) and b) a DNP surface at equilibrium in water (purple) and C12E5 (red). After 17 bubbles, the DNP surface failed to induce bubble rupturing within 2 min. Bubbles remained pinned on the surface (red area). c) Roll-off angles using 6 μL of *n*-hexadecane, water, and C12E5 before and after conducting single-bubble rupture experiments in C12E5 on LFS (blue) and DNP (orange). SEM images of the d,e) LFS and f,g) DNP surface before (d,f) and after (e,g) conducting experiments in C12E5 (scale bars are 2 μm).

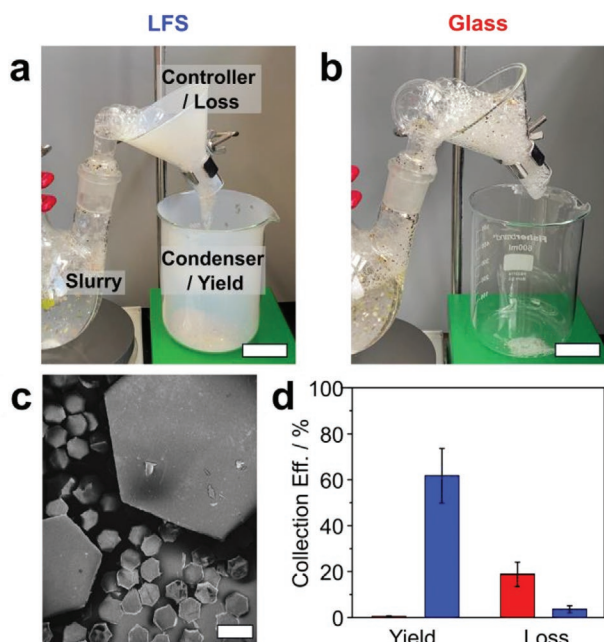


Figure 5. Separation of solid plates via froth flotation using a) a LFS coated and b) a pristine glass froth controller and condenser (scale bars are 5 cm). Froth produced from the slurry composed of C12E5 in water and hydrophobized hexagonal PET plates via a stirrer, is transported along the froth controller to the condenser. The setup was run for 2 min of a) continuous and b) pulsed flotation. c) The size distribution (tip-to-tip) of the solid component is 1:1:1 w/w/w of 2600, 1200, and 250 μm . d) The high material collection yield demonstrates the potential of superamphiphobic froth control systems. While the glass control suffers from clogging and losses at the outlet, the superamphiphobic system experiences minimal clogging and no losses.

of low interfacial tension offers the possibility to destabilize bubbles in froth flotation, a heterogeneous mixture of a liquid, a gas, and a solid phase. Flotation has long been used to selectively separate solid materials using stable froths from a slurry generated, for example, in industrial wastewater treatment^[8,9] and mineral processing.^[10,11] Froth flotation efficiency is gauged with respect to froth collection, production efficiency, and the purity of the “final concentrate”.^[45]

Here, we demonstrate the separation efficiency of both, a LFS coated (Figure 5a) and an uncoated (Figure 5b) froth controller and condenser. The uncoated device serves as a control. The LFS coated, liquid-repellent froth controller, hereafter also called delivery channel is used to freely transport the complex three-component mixture to the froth condenser. Here, the foam is still draining and the bubbles are transported on a thin layer of surfactant solution. In the froth condenser, the foam bubbles are burst upon contact with the structured side-walls of the beaker. The froth was generated via stirring from 400 mL of an aqueous slurry composed of C12E5 (1.0 mM) and 600 mg of hydrophobized PET plates^[46] (Figure 5c) with an air inlet pressure of 0.3 bar. The setup was run for 2 min of continuous and pulsed flotation (Video M4, Supporting Information). The control runs had to be pulsed to prevent excessive spillage during froth/particle collection. In contrast, the superamphiphobic system demonstrated 1) continuous flotation due

to efficient bubble transport and rupturing by both the froth controller and condenser, 2) successful particle collection with high yields of $61 \pm 11\%$, and 3) minimal delivery channel (i.e., funnel) losses. The uncoated device exhibited low yields of only $1 \pm 1\%$ with excessive particle clogging and losses ($19 \pm 5\%$) within the delivery channel.

3. Conclusion

In conclusion, ultrafast bubble bursting by superamphiphobic surfaces requires control of the nano- and micrometer-scale architecture of the hierarchical structures. Superhydrophobicity, superamphiphobicity, and even aerophilicity do not automatically guarantee efficient bubble rupturing capabilities. LFS is a highly tunable technique, suitable for the design of hierarchical textures with optimized length scale, network geometry, and particle diameters below 100 nm to induce so-called ultrafast bubble bursting in less than 2 ms. The surfaces demonstrate long-term bubble rupturing properties without chemical or mechanical degradation in both pure water and surfactant solution. Therefore, LFS serves as a promising candidate for passive bubble capturing. We demonstrated the use of superamphiphobic coatings for froth control by enhancing the efficiency of a flotation setup. We envision the use of these optimal design principles for applications in industrial water treatment, foam control, and electrocatalytic gas-evolving reactions for clean energy production.

4. Experimental Section

Liquid Flame Spray Coatings: A flame was created by oxygen (2 L min^{-1}) and methane (1 L min^{-1}). A liquid feedstock consisting of TEOS (98 %, Sigma Aldrich) dissolved in isopropanol (Fisher Scientific) was dispersed into the flame using oxygen (5 L min^{-1}) at a feed rate of 1 mL min^{-1} . The concentration of TEOS in isopropanol was 370 mg mL^{-1} . The distance between the burner unit and the glass substrate was varied from 22 to 52 cm, the maximum distance accessible. The coating time was varied from 3, to 5 and 10 min. To enhance the mechanical stability of the particle coatings, a silica shell was added via CVD. The surfaces were placed in a desiccator together with TEOS (98 %, Sigma Aldrich, 2 mL in 2.400 cm^3) and aqueous ammonia solution (25 %, VWR Chemicals, 2 mL in 2.400 cm^3). The reaction was allowed to proceed for 16 h at atmospheric pressure. Thereafter, the coatings were sintered for 3 h at $500 \text{ }^\circ\text{C}$ in air. The surfaces were fluorinated using 100 μL 1H,1H,2H,2H-perfluorooctyl-trichlorosilane (PFOTS, 97 %, Alfa Aesar) in a desiccator (9.200 cm^3) at 50 mbar. After 2 h, the surfaces were removed and placed into a vacuum oven at $60 \text{ }^\circ\text{C}$ for 2 h to remove unreacted silane.

Dense Nanoparticle Coatings: The particle spray coating was synthesized according to the procedure described by Wong et al.^[29] The synthesis was conducted under argon atmosphere. Under gentle stirring, 1 g of fumed silica nanoparticles (Aldrich, 7 nm, SSA = $395 \text{ m}^2 \text{ g}^{-1}$) and 0.9 mL of 1H,1H,2H,2H-perfluorooctyl-trichlorosilane were added to 30 mL of dried chloroform (> 99.8 %, Fisher Scientific). The reaction was allowed to proceed at $25 \text{ }^\circ\text{C}$ and a stirring rate of 500 rpm for 96 h. Afterwards, the particles were washed with chloroform and dried at $50 \text{ }^\circ\text{C}$ for 24 h. For spray coating, the particles were re-dispersed in acetone at a concentration of 10 mg mL^{-1} . 10 mL of the suspension were used to coat an area of $76 \times 26 \text{ mm}$. The suspension was sprayed onto a microscope glass slide with a flow rate of 0.2 mL s^{-1} at 3 bars and a working distance of 10 cm using a spray gun (nozzle diameter of 0.2 mm). The surfaces were allowed to dry for 24 h.

Silicone Nanofilaments: A mixture of TCMS (400 μL , 99 %, Sigma Aldrich) and toluene (100 mL, Sigma Aldrich) with a water content between 150 and 170 ppm was stirred for 60 s. The water content was evaluated using a coulometer (Mettler Toledo C20 Compact KF coulometer). Microscope glass slides (Thermo Scientific) were immersed into the solution and the reaction vessel was tightly sealed. After 3 h, the surfaces were briefly washed with hexane (95 %, Fisher Scientific) and dried under a nitrogen flow. The nanofilaments were activated with oxygen plasma (Diener Electronic Femto, 6 $\text{cm}^3 \text{min}^{-1}$ oxygen flow rate) for 2 min at 120 W. Thereafter, the surfaces were placed in a desiccator (9.200 cm^3) together with 100 μL PFOTS (97 %, Alfa Aesar). The pressure was reduced to 50 mbar and the reaction was allowed to proceed for 2 h at room temperature. Afterwards, the surfaces were placed in a vacuum oven for 2 h at 60 $^\circ\text{C}$.

Characterization: The roll-off angles were measured using water, *n*-hexadecane, and C12E5 (0.03 mm, CMC: 0.07 mm at 25 $^\circ\text{C}$).^[44] The surface tensions were 72.8, 27.5, and 30.7 mN m^{-1} ,^[44] respectively. Roll-off angles were measured by carefully placing a 6 μL droplet onto the surface and subsequently tilting the surface at a rate of 1 degree per second until the droplet slides completely out of the field of view. A minimum of 5 spots was analyzed for each surface. Scanning electron microscopy (SEM) images were acquired at a voltage of 3 kV (InLens Detector, LEO 1530 Gemini, Zeiss). To reduce charging effects and enhance the image quality, surfaces were coated with a 9 nm Pt layer (BalTec MED 020 Modular High Vacuum Coating System, Argon at 2×10^{-2} mbar and 30 mA). For the particle size distributions, a minimum of 100 particles per surface was evaluated using ImageJ. Dynamics of single bubble rupturing were recorded using a high-speed camera (Fastcam AX10, Photron) and a high magnification objective (2x, Mitutoyo) at a frame rate of 20 000 frames per second. Bubble mobility was analyzed using image processing algorithms in MATLAB (edge detection). This enabled tracking of bubbles and their respective center-of-mass. The velocity of the center-of-mass was computed, and used to determine key events: 1) Initial decrease to minimum represents surface approach, 2) Sharp increase to maximum represents rupture, and 3) Final decrease from maximum triggers the end of the analysis.

Supporting Information

Supporting Information is available from the Wiley Online Library or from the author.

Acknowledgements

The authors thank H.-J. Butt, L. Hauer, A. Naga, and A. Sharifi for stimulating discussions and technical support. This work was supported by the Max Planck Graduate Center (K.I.H.), the European Union's Horizon 2020 research and innovation program LubISS No. 722497 (W.S.Y.W., D.V.), and the ERC Advanced Grant No. 340391 "SUPRO" and the priority program SPP 2171 (D.V.).

Open access funding enabled and organized by Projekt DEAL.

Conflict of Interest

The authors declare no conflict of interest.

Data Availability Statement

The data that supports the findings of this study are available in the supplementary material of this article.

Keywords

aerophilic surfaces, bubble bursting, bubble rupturing, defoaming, flotation, liquid flame spray, superamphiphobic surfaces

Received: March 9, 2021

Revised: May 12, 2021

Published online:

- [1] A. Angulo, P. van der Linde, H. Gardeniers, M. Modestino, D. F. Rivas, *Joule* **2020**, 4, 555.
- [2] J.-H. Kim, J. P. Rothstein, *Exp. Fluids* **2016**, 57, 81.
- [3] Z. Long, Y. Zhao, C. Zhang, Y. Zhang, C. Yu, Y. Wu, J. Ma, M. Cao, L. Jiang, *Adv. Mater.* **2020**, 32, 1908099.
- [4] Y. Luo, L. Tang, U. Khan, Q. Yu, H. M. Cheng, X. Zou, B. Liu, *Nat. Commun.* **2019**, 10, 269.
- [5] S. I. Karakashev, M. V. Grozdanova, *Adv. Colloid Interface Sci.* **2012**, 176–177, 1.
- [6] H. Leuner, C. Gerstenberg, K. Lechner, C. McHardy, C. Rauh, J. U. Repke, *Chem. Eng. Res. Des.* **2020**, 163, 281.
- [7] Y. Xing, X. Gui, L. Pan, B. El Pinchasik, Y. Cao, J. Liu, M. Kappl, H. J. Butt, *Adv. Colloid Interface Sci.* **2017**, 246, 105.
- [8] J. Rubio, M. L. Souza, R. W. Smith, *Miner. Eng.* **2002**, 15, 139.
- [9] C. Y. Teh, P. M. Budiman, K. P. Y. Shak, T. Y. Wu, *Ind. Eng. Chem. Res.* **2016**, 55, 4363.
- [10] Z. Wu, X. Wang, H. Liu, H. Zhang, J. D. Miller, *Adv. Colloid Interface Sci.* **2016**, 235, 190.
- [11] A. P. Chandra, A. R. Gerson, *Adv. Colloid Interface Sci.* **2009**, 145, 97.
- [12] L. Rapoport, T. Emmerich, K. K. Varanasi, *Adv. Mater. Interfaces* **2020**, 7, 2070029.
- [13] J. Wang, Q. Yang, M. Wang, C. Wang, L. Jiang, *Soft Matter* **2012**, 8, 2261.
- [14] A. Kannan, P. Hristov, J. Li, J. Zawala, P. Gao, G. G. Fuller, *J. Colloid Interface Sci.* **2020**, 575, 298.
- [15] H. De Maleprade, C. Clanet, D. Quéré, *Phys. Rev. Lett.* **2016**, 117, 094501.
- [16] C. Shi, X. Cui, X. Zhang, P. Tchoukov, Q. Liu, N. Encinas, M. Paven, F. Geyer, D. Vollmer, Z. Xu, H. -J. Butt, H. Zeng, *Langmuir* **2015**, 31, 7317.
- [17] J. Huo, Q. Yang, J. Yong, P. Fan, Y. feng Lu, X. Hou, F. Chen, *Adv. Mater. Interfaces* **2020**, 7, 1902128.
- [18] J. Wang, Y. Zheng, F. Q. Nie, J. Zhai, L. Jiang, *Langmuir* **2009**, 25, 14129.
- [19] D. Y. C. Chan, E. Klaseboer, R. Manica, *Soft Matter* **2011**, 7, 2235.
- [20] H. Teisala, F. Geyer, J. Haapanen, P. Juuti, J. M. Mäkelä, D. Vollmer, H. J. Butt, *Adv. Mater.* **2018**, 30, 1706529.
- [21] W. S. Y. Wong, G. Liu, N. Nasiri, C. Hao, Z. Wang, A. Tricoli, *ACS Nano* **2017**, 11, 587.
- [22] H. K. Kammler, L. Mädler, S. E. Pratsinis, *Chem. Eng. Technol.* **2001**, 24, 583.
- [23] L. Mädler, H. K. Kammler, R. Mueller, S. E. Pratsinis, *J. Aerosol Sci.* **2002**, 33, 369.
- [24] H. K. Park, K. Y. Park, *KONA Powder Part. J.* **2015**, 32, 85.
- [25] H. J. Butt, C. Semperebon, P. Papadopoulos, D. Vollmer, M. Brinkmann, M. Ciccotti, *Soft Matter* **2013**, 9, 418.
- [26] Z. Chu, S. Seeger, *Chem. Soc. Rev.* **2014**, 43, 2784.
- [27] X. Deng, L. Mammen, H. J. Butt, D. Vollmer, *Science* **2012**, 335, 67.
- [28] A. Tuteja, W. Choi, M. Ma, J. M. Mabry, S. A. Mazzella, G. C. Rutledge, G. H. McKinley, R. E. Cohen, *Science* **2007**, 318, 1618.
- [29] W. S. Y. Wong, *Nano Lett.* **2019**, 19, 1892.
- [30] J. Zhang, S. Seeger, *Angew. Chem., Int. Ed.* **2011**, 50, 6652.
- [31] G. R. J. Artus, S. Jung, J. Zimmermann, H. P. Gautschi, K. Marquardt, S. Seeger, *Adv. Mater.* **2006**, 18, 2758.

- [32] R. Mueller, R. Jossen, H. K. Kammler, S. E. Pratsinis, M. K. Akhtar, *AIChE J.* **2004**, *50*, 3085.
- [33] F. Meierhofer, L. Mädler, U. Fritsching, *AIChE J.* **2020**, *66*, e16885.
- [34] N. Nasiri, T. D. Elmøe, Y. Liu, Q. H. Qin, A. Tricoli, *Nanoscale* **2015**, *7*, 9859.
- [35] L. Mädler, A. A. Lall, S. K. Friedlander, *Nanotechnology* **2006**, *17*, 4783.
- [36] S. N. Rogak, R. C. Flagan, H. V. Nguyen, *Aerosol Sci. Technol.* **1993**, *18*, 25.
- [37] M. Paven, R. Fuchs, T. Yakabe, D. Vollmer, M. Kappl, A. N. Itakura, H. J. Butt, *Adv. Funct. Mater.* **2016**, *26*, 4914.
- [38] G. C. Frye, J. C. Berg, *J. Colloid Interface Sci.* **1989**, *127*, 222.
- [39] O. Reynolds, *Philos. Trans. R. Soc. London* **1886**, *177*, 157.
- [40] A. Dippenaar, *Int. J. Miner. Process.* **1982**, *9*, 1.
- [41] D. Schäffel, K. Koynov, D. Vollmer, H. J. Butt, C. Schönecker, *Phys. Rev. Lett.* **2016**, *116*, 134501.
- [42] B. Liu, R. Manica, Q. Liu, E. Klaseboer, Z. Xu, G. Xie, *Phys. Rev. Lett.* **2019**, *122*, 194501.
- [43] D. Georgieva, A. Cagna, D. Langevin, *Soft Matter* **2009**, *5*, 2063.
- [44] F. Henrich, D. Fell, D. Truskowska, M. Weirich, M. Anyfantakis, T. H. Nguyen, M. Wagner, G. K. Auernhammer, H. J. Butt, *Soft Matter* **2016**, *12*, 7782.
- [45] A. Bahrami, Y. Ghorbani, M. R. Hosseini, F. Kazemi, M. Abdollahi, A. Danesh, *Miner. Eng.* **2019**, *71*, 43.
- [46] F. Geyer, Y. Asaumi, D. Vollmer, H. J. Butt, Y. Nakamura, S. Fujii, *Adv. Funct. Mater.* **2019**, *29*, 1808826.